Thermal lattice Boltzmann simulation for multispecies fluid equilibration

Linda Vahala
Department of Electrical and Computer Engineering, Old Dominion University, Norfolk, Virginia 23529

Darren Wah* and George Vahala
Department of Physics, William and Mary College, Williamsburg, Virginia 23187

Jonathan Carter
NERSC, Lawrence Berkeley Laboratory, Berkeley, California 97320

Pavol Pavlo
Institute of Plasma Physics, Czech Academy of Science, Praha 8, Czech Republic
(Received 13 January 2000)

The equilibration rate for multispecies fluids is examined using thermal lattice Boltzmann simulations. Two-dimensional free-decay simulations are performed for effects of velocity shear layer turbulence on sharp temperature profiles. In particular, parameters are so chosen that the lighter species is turbulent while the heavier species is laminar—and so its vorticity layers would simply decay and diffuse in time. With species coupling, however, there is velocity equilibration followed by the final relaxation to one large co- and one large counter-rotating vortex. The temperature equilibration proceeds on a slower time scale and is in good agreement with the theoretical order of magnitude estimate of Morse [Phys. Fluids **6**, 1420 (1963)].

PACS number(s): 47.11.+j

I. INTRODUCTION

The physics of the relaxation processes for multispecies fluids/gases has long been of interest [1–8]. A recent interest in multispecies relaxation has been spurred on by the need to develop schemes that can cope with the wide range of collisionalities encountered in the outer regions of a tokamak [8] (the so-called ''scrape-off layer''). Under certain conditions, it has been argued [9] that there can be three time scales of interest in the relaxation of a multispecies system to a final thermodynamic equilibrium state. On the fastest time scale is the relaxation of the lighter species to a thermal distribution centered around the mean velocity of the heavier species. The next time scale has the heavier species relaxing to a thermal distribution on a time scale greater by a factor of the square root of the mass ratio. The longest time scale is that on which the light species and heavier species temperatures equilibrate. Of particular interest is an order-of-magnitude estimate of the ratio of the time for the species temperature difference to become negligible to the time for the species mean velocity difference to become negligible. Under some simplifying assumptions, and for spatially homogeneous systems, this ratio scales as [1]

$$\frac{\tau_{\Delta\theta}}{\tau_{\Delta\nu}} \approx \frac{1}{2}\left(\frac{n_1 m_1 + n_2 m_2}{n_1 + n_2}\right)\left(\frac{m_1 + m_2}{m_1 m_2}\right) \geqslant 1, \qquad (1)$$

where n_s, m_s are the density and mass of the sth species and irrespective of whether one is considering Maxwell, hard sphere, or Coulomb interactions. If $m_1 \neq m_2$, then $\tau_{\Delta T} > \tau_{\Delta\nu}$.

Here, we shall examine the relaxation of a two-fluid two-dimensional (2D) turbulent system in which each species initially has a double velocity shear layer—with one species shear layer being perpendicular to that of the other. Thus initially, species 1 has vorticity dependence only in the x direction, $\omega_1(x)$, while fluid 2 has $\omega_2 = \omega_2(y)$ only. Moreover, initially, each species is assumed to have a sharp temperature profile—with $\theta_1 = \theta_1(x)$ and $\theta_2 = \theta_2(y)$ only.

In the highly collisional regime of interest here, a two-species nonlinear fluid description is valid. To achieve a quantitative solution to the relaxation problem one must resort to numerical techniques. In the conventional (direct) approach to solving the coupled macroscopic conservation equations of mass, momentum, and energy for each species, one would have to accurately resolve the nonlinear convective derivatives. This Riemann problem is computationally quite expensive and readily consumes over 30% of the run time. Here, instead of applying the conventional approach, we shall introduce a kinetic lattice method, which, because of the higher phase dimensionality, will obviate the Riemann problem entirely. In particular, we shall consider a thermal lattice Boltzmann model [9–17] (TLBM). TLBMs are very appealing since they are (a) computationally more efficient than conventional Navier-Stokes solvers and are (b) ideal for parallel processors. The first hurdle that the TLBM must overcome is the extra computational expense incurred by increasing the phase space dimensionality, which for a collision-dominated regime seems to be an inverse statistical mechanical description. However, this embedding into a higher dimensional phase space has potential advantages that can be exploited. In particular, in the fluid limit, the exact

*Present address: High Performance Technologies, Aberdeen, MD 21001.

form of the collision operator is not critical. Hence one can introduce, for example, the linear Bhatnagar-Gross-Krook [18] (BGK) operator instead of the complicated full nonlinear Boltzmann operator [1–4]. The beauty of the BGK collision operator is that it is amenable to efficient numerics without sacrificing any of the essential continuum physics [1–5]. TLBM is intimately tied to the kinetic phase space velocity lattice on which it will be solved. In particular, TLBM is a maximally discretized molecular dynamics since one attempts to minimize the number of discrete molecular speeds needed to recover the correct fluid equations. The TLBM algorithm proceeds in three basic steps: (a) free-stream the distribution function to different lattice sites according to the lattice velocity vectors; (b) recompute macroscopic quantities at each nodal site; and (c) perform BGK collisional relaxation at each node. Thus the TLBM results in a very simple, efficient, and ideally parallel algorithm since step (a) is a simple shift (advection) operator, while steps (b) and (c) require information that is purely local at that node. Having extolled the strengths of the TLBM one would be amiss not to point out its well-known inherent weakness—that of numerical instability [10–13]. Let it suffice that work is still in progress in combating this Achilles' heel and some preliminary results will be reported elsewhere [19]. Meanwhile we deem it prudent to restrict ourselves to examining 2D turbulence—even though 3D models [12,15,16] are available, they are substantially more expensive computationally (while not increasing the numerical stability regimes).

In Sec. II the two-fluid nonlinear equations are presented as well as the two-species linear BGK kinetic equations which will, under standard Chapman-Enskog expansions, reduce to the given macroscopic system. In Sec. III the equilibration of different species velocities and temperatures and final velocity relaxation is examined for 2D turbulent double shear layers, while we make some final comments in Sec. IV.

II. MULTIFLUID SYSTEM

Consider the two-fluid system described by the following conservation equations of mass, momentum, and energy:

$$\frac{\partial}{\partial t}(m_s n_s)+\frac{\partial}{\partial x_\alpha}(m_s n_s \nu_{s,\alpha})=0, \tag{2}$$

$$\frac{\partial}{\partial t}(m_s n_s \nu_{s,\alpha})+\frac{\partial}{\partial x_\beta}(m_s n_s \nu_{s,\beta}\nu_{s,\alpha}) = -\frac{\partial \Pi_{s,\alpha\beta}}{\partial x_\beta}-\frac{m_s n_s}{\tau_{s,s'}}(\nu_{s,\alpha}-\nu_{ss',\alpha}), \tag{3}$$

$$\frac{\partial}{\partial t}(3n_s\theta_s+m_s n_s \mathbf{v}_s^2)+\frac{\partial}{\partial x_\alpha}(\nu_{s,\alpha}[3n_s\theta_s+m_s n_s \mathbf{v}_s^2]) = -\frac{\partial}{\partial x_\alpha}(2q_{s,\alpha}+2\nu_{s,\beta}\Pi_{s,\alpha\beta})-\frac{1}{\tau_{ss'}}[3n_s(\theta_s-\theta_{ss'}) + m_s n_s(\mathbf{v}_s^2-\mathbf{v}_{ss'}^2)]. \tag{4}$$

m_s, n_s, $\mathbf{v}_s$, θ_s are the mass, density, velocity and temperature of the sth species. The sth species stress tensor Π_s is defined by

$$\Pi_{s,\alpha\beta}=n_s\theta_s\delta_{\alpha\beta}-\mu_s\left(\left[\frac{\partial \nu_{s,\alpha}}{\partial x_\beta}+\frac{\partial \nu_{s,\beta}}{\partial x_\alpha}\right]-\frac{2}{3}\nabla\cdot\mathbf{v}_s\delta_{\alpha\beta}\right) + m_s n_s\frac{\tau_s}{\tau_{ss'}}\left[\left\{\frac{\theta_{ss'}-\theta_s}{m_s}-\frac{(\mathbf{v}_{ss'}-\mathbf{v}_s)^2}{s}\right\}\delta_{\alpha\beta} + (\nu_{ss',\alpha}-\nu_{s,\alpha})(\nu_{ss',\beta}-\nu_{s,\beta})\right], \tag{5}$$

while the sth species heat flux vector

$$q_{s,\alpha}=-\kappa_s\frac{\partial\theta_s}{\partial x_\alpha}+\frac{5}{2}n_s\frac{\tau_s}{\tau_{ss'}}(\theta_s-\theta_{ss'})(\nu_{s,\alpha}-\nu_{ss',\alpha}) -\frac{1}{2}m_s n_s(\mathbf{v}_s-\mathbf{v}_{ss'})^2(\nu_{s,\alpha}-\nu_{ss',\alpha}). \tag{6}$$

τ_s and $\tau_{ss'}$ are the sth species and cross-species relaxation rates, while μ_s and κ_s are the sth species viscosity and conductivity coefficients. The effects of cross-species interactions on the momentum and energy equations are apparent in the right-hand sides of (3) and (4). The convention of summing over repeated (Greek) subscripts is employed here. For simplicity, we do not incorporate effects of sources/sinks in the sth particle mass conservation equations.

A. Kinetic description of a multifluid system

The conservation equations (3)–(6) can readily be derived from a simplified two-species kinetic description [2]. In particular, these macroscopic moment equations are readily derived by a straightforward Chapman-Enskog expansion [3] on the sth species linearized BGR [10] for the distribution function $f_s(\mathbf{x},\xi,t)$

$$\frac{\partial f_s}{\partial t}+\frac{\partial}{\partial x_\alpha}(\xi_\alpha f_s)=-\frac{f_s-g_s}{\tau_s}-\frac{f_s-g_{ss'}}{\tau_{ss'}}. \tag{7}$$

The sth species relaxation distribution function (for 2D flows) is

$$g_s=n_s\frac{m_s}{2\pi\theta_s}\exp\left[-\frac{m_s(\xi-\mathbf{v}_s)^2}{2\theta_s}\right], \tag{8}$$

while the cross-species relaxation distribution function is

$$g_{ss'}=n_s\frac{m_s}{2\pi\theta_{ss'}}\exp\left[-\frac{m_s(\xi-\mathbf{v}_{ss'})}{2\theta_{ss'}}\right]. \tag{9}$$

The cross-species parameters $\mathbf{v}_{ss'}$ and $\theta_{ss'}$ as well as the cross-species relaxation parameters $\tau_{ss'}$ satisfy certain physical constraints based on the relaxation physics. Here, we follow Greene [5] and impose the typical plasma species relaxation rates

$$m_s n_s \tau_{s's}=m_{s'}n_{s'}\tau_{ss'}. \tag{10}$$

Of course, other cross-species relaxation rates could be evoked, provided they do not violate the physics: The

heavier species should not relax on the fastest time scale and both species, irrespective of their mass, should be equally affected by their mutual collisions. Moreover, the cross-species collisions are chosen to conserve species densities, as well as momentum and energy. In particular, for collisional momentum conservation,

$$0=\int d\xi\, m_s\xi\left[-\frac{f_s-g_s}{\tau_s}-\frac{f_s-g_{ss'}}{\tau_{ss'}}\right]+\int d\xi m_{s'}\xi \times\left[-\frac{f_{s'}-g_{s'}}{\tau_{s'}}-\frac{f_{s'}-g_{s's}}{\tau_{s's}}\right] =\frac{m_s n_s}{\tau_{ss'}}(\mathbf{v}_{ss'}-\mathbf{v}_s)+\frac{m_{s'}n_{s'}}{\tau_{s's}}(\mathbf{v}_{s's}-\mathbf{v}_{s'}).$$

Assuming the cross-species relaxation rates satisfy Eq. (10), the collisional momentum conservation then requires

$$\mathbf{v}_{ss'}-\mathbf{v}_s+\mathbf{v}_{s's}-\mathbf{v}_{s'}=0. \tag{11}$$

Similarly, the collisional energy conservation [under the cross-species relaxation rate Eq. (10)] requires

$$\left(\frac{\theta_{s's}-\theta_{s'}}{m_{s'}}\right)+\frac{1}{3}(\mathbf{v}_{s's}^2-\mathbf{v}_{s'}^2)+\left(\frac{\theta_{ss'}-\theta_s}{m_s}\right)+\frac{1}{3}(\mathbf{v}_{ss'}^2-\mathbf{v}_s^2)=0. \tag{12}$$

The macroscopic variables n_s, $\mathbf{v}_s$, θ_s are defined by the standard moments

$$n_s=\int d\xi f_s;\quad n_s\mathbf{v}_s=\int d\xi f_s\xi;\quad 2n_s\theta_s=\int d\xi f_s\xi^2-n_s\mathbf{v}_s^2. \tag{13}$$

For 2D flows, Eqs. (11) and (12) place three constraints on the six parameters $\mathbf{v}_{ss'}$, $\mathbf{v}_{s's}$, $\theta_{ss'}$, $\theta_{s's}$ introduced in the cross-species relaxation distribution function, Eq. (9).

Further constraints on these parameters are obtained when we require that the equilibration rates for the species velocity and temperature

$$\frac{\partial}{\partial t}(\mathbf{v}_s-\mathbf{v}_{s'})\ \text{ and }\ \frac{\partial}{\partial t}(\theta_s-\theta_{s'})$$

have the same functional form in the BGK formalism as with the full nonlinear Boltzmann collisional integrals. These constraints are quite complicated and the interested reader should consult the details in Morse [1] and Greene [5]. Suffice it to say, and as Green [3] has pointed out, that these constraints do not determine the six parameters $\mathbf{v}_{ss'}$, $\mathbf{v}_{s's}$, $\theta_{ss'}$, $\theta_{s's}$ uniquely because of a redundancy. This redundancy allows the introduction of a free parameter [3] β with

$$\mathbf{v}_{ss'}=\frac{\mathbf{v}_s+\mathbf{v}_{s'}}{2}-\frac{\beta(\mathbf{v}_s-\mathbf{v}_{s'})}{2},$$

$$\mathbf{v}_{s's}=\frac{\mathbf{v}_s+\mathbf{v}_{s'}}{2}+\frac{\beta(\mathbf{v}_s-\mathbf{v}_{s'})}{2},$$

$$\theta_{ss'}=\frac{m_{s'}\theta_s+m_s\theta_{s'}}{m_s+m_{s'}}-\beta\frac{m_s(\theta_s-\theta_{s'})}{m_s+m_{s'}}+\frac{(1-\beta^2)}{6}\frac{m_s m_{s'}}{m_s+m_{s'}}(\mathbf{v}_s-\mathbf{v}_{s'})^2+\frac{(1+\beta)^2}{12}\frac{m_{s'}-m_s}{m_s+m_{s'}}m_s(\mathbf{v}_s-\mathbf{v}_{s'})^2,$$

$$\theta_{s's}=\frac{m_{s'}\theta_s+m_s\theta_{s'}}{m_s+m_{s'}}+\beta\frac{m_s(\theta_s-\theta_{s'})}{m_s+m_{s'}}+\frac{(1-\beta^2)}{6}\frac{m_s m_{s'}}{m_s+m_{s'}}(\mathbf{v}_s-\mathbf{v}_{s'})^2-\frac{(1+\beta)^2}{12}\frac{m_{s'}-m_s}{m_s+m_{s'}}m_{s'}(\mathbf{v}_s-\mathbf{v}_{s'})^2. \tag{14}$$

For the problem we are considering, the self-species collisional relaxation is taken to be that for hard spheres [1,2]

$$\tau_s\approx\frac{1}{n_s}\left(\frac{m_s}{\theta_s}\right)^{1/2}, \tag{15}$$

and the cross-species collisional relaxation [1,2]

$$\tau_{ss'}=\frac{1+\beta}{\alpha_{ss'}}\frac{n_s m_s}{m_s+m_{s'}}\gg\tau_s \tag{16}$$

with $\beta>-1$ arbitrary, and $\alpha_{ss'}$

$$\alpha_{ss'}=\alpha_{s's}\approx\frac{m_s m_{s'}}{(m_s+m_{s'})^2}n_s n_{s'}\left(\frac{\beta_s}{m_s}+\frac{\theta_{s'}}{m_{s'}}\right)^{1/2}. \tag{17}$$

The 2D transport coefficients in Eqs. (5) and (6) are readily determined using standard Chapman-Enskog techniques on Eq. (7): the sth species viscosity $\mu_s=\tau_s n_s\theta_s$ and the heat conductivity $\kappa_s=2\tau_s n_s\theta_s$.

B. TLBM for a two-species system

On discretizing the phase space velocity ξ, the continuum distribution function $f_s(\mathbf{x},\xi,t)$ will be denoted by $N_{spi}(\mathbf{x},t)$:

$$f_s(\mathbf{x},\xi,t)\rightarrow N_{spi}(\mathbf{x},t), \tag{18}$$

where the subscript i denotes the lattice links to that particular spatial node $\mathbf{x}$ and p denotes the different lattice speeds required in order to recover the given macroscopic equations (2)–(6). The range of values these subscripts take is totally dependent on the particular velocity lattice chosen as well as the level of moment closures besides the rest particle, $p=0$.

Some 2D lattices	Isothermal model	Thermal model
Square lattice	$i=1,...,4,\ p=1,\sqrt{2}$	$i=1,...,4,\ p=1,\sqrt{2},2$
Hexagonal lattice	$i=1,...,6,\ p=1$	$i=1,...,6,\ p=1,2$
Octagonal lattice	$i=1,...,8,\ p=1$	$i=1,...,8,\ p=1,2$

In essence, this table gives the total phase space velocity information that is needed at each spatial node in the TLBM in order to recover the full fluid conservation equations of

interest. Thus for energy closure on a hexagonal grid, one requires only 13 real numbers of ξ information at each spatial node.

The TLBM, in its simplest form, is first order in time and second order in space discretization of the continuum BGK equations (7):

$$N_{1p_i}(\mathbf{x}+\mathbf{c}_{pi},t+1)-N_{1pi}(\mathbf{x},t) = -\frac{1}{\tau_1}[N_{1pi}(\mathbf{x},t)-N^{eq}_{1pi}(\mathbf{x},t)] - \frac{1}{\tau_{12}}[N_{1pi}(\mathbf{x},t)-N^{eq}_{12pi}(\mathbf{x},t)], \tag{19}$$

$$N_{2pi}(\mathbf{x}+\mathbf{c}_{pi},t+1)-N_{2pi}(\mathbf{x},t) = -\frac{1}{\tau_2}[N_{2pi}(\mathbf{x},t)-N^{eq}_{2pi}(\mathbf{x},t)] - \frac{1}{\tau_{21}}[N_{2pi}(\mathbf{x},t)-N^{eq}_{21pi}(\mathbf{x},t)]. \tag{20}$$

Equations (19) and (20) are written in TLBM units of $\delta t=1$ and $\delta x=1$. $\mathbf{c}_{pi}$ is the kinetic velocity lattice vector, with $\mathbf{c}_{pi}=p\mathbf{c}_i$, and $|\mathbf{c}_i|=1$. Before specifying the relaxation distributions N^{eq} in detail, we note that from Chapman-Enskog theory that N^{eq}_{spi}, $N^{eq}_{ss'pi}$ can only be functions of the macroscopic variables $n_s,\mathbf{v}_s,\theta_s$ and $n_{s'},\mathbf{v}_{s'},\theta_{s'}$, where

$$n_s=\sum_{pi} N_{spi}, \quad n_s\mathbf{v}_s=\sum_{pi} N_{spi}\mathbf{c}_{pi},$$

$$2n_s\theta_s=\sum_{pi} N_{spi}\mathbf{c}^2_{pi}-n_s\mathbf{v}^2_s. \tag{21}$$

At each lattice site $\mathbf{x}$, the TLBM algorithm to propagate N_{spi} from time $t\rightarrow t+1$ is (a) free-stream the distribution $N_{spi}(\mathbf{x})\rightarrow N_{spi}(\mathbf{x}+\mathbf{c}_{pi})$; (b) recalculate the macroscopic variables $n_s,\mathbf{v}_s,\theta_s$ using Eq. (21) and update all the N^{eq}; (c) perform collisional relaxation at each lattice node:

$$N_{spi}(\mathbf{x})-\frac{1}{\tau_s}[N_{spi}(\mathbf{x})-N^{eq}_{spi}(\mathbf{x})]-\frac{1}{\tau_{ss'}}[N_{spi}(\mathbf{x}) - N^{eq}_{ss'pi}(\mathbf{x})]\Rightarrow N_{spi}(\mathbf{x}) \quad \text{at time } t+1.$$

One immediately notes that (a) is a simple shift operation numerically, while (b) and (c) require only local data at the spatial node site $\mathbf{x}$. Thus the algorithm is ideal for multiparallel processing elements and more details on the message passing interface parallelization can be found in Ref. [9]. Moreover, the shift operation in (a) implies that we are running at a kinetic Courant-Fredricks-Levy number CFL=1. This implies no numerical dissipation or diffusion is introduced. It is precisely these properties of the TLBM that make it so attractive as an alternative to the normal computational fluid dynamic approach. From the discrete Chapman-Enskog procedure [20], it has been shown that the transport coefficients are augmented by a $\frac{1}{2}$ factor:

$$\mu_s=(\tau_s-\tfrac{1}{2})n_s\theta_s, \quad \kappa_s=2(\tau_s-\tfrac{1}{2})n_s\theta_s.$$

However, the numerical stability of the TLBM rests on the specification of the relaxed distribution functions N^{eq}. Typically, these N^{eq} are taken to have the form

$$N^{eq}_{spi}=A_{sp}(\theta_{sp})+B_{sp}(\theta_s)\mathbf{c}_{pi}\cdot\mathbf{v}_s+C_{sp}(\theta_s)\{\mathbf{c}_{pi}\cdot\mathbf{v}_s\}^2 + D_{sp}(\theta_s)\mathbf{v}^2_s+E_{sp}(\theta_s)\{\mathbf{c}_{pi}\cdot\mathbf{v}_s\}\mathbf{v}^2_s + F_{sp}(\theta_s)\{\mathbf{c}_{pi}\cdot\mathbf{v}_s\}^3+\cdots \tag{22}$$

and a similar form for the cross-species $N^{eq}_{ss',pi}$ where one now replaces $n_s,\mathbf{v}_s,\theta_s$ by the cross-species variables $n_{ss'},\mathbf{v}_{ss'},\theta_{ss'}$ as defined in Eq. (17). One truncates these Taylor expansions in $\mathbf{v}_s,\theta_s$ depending on the moment level closure invoked. The following (infinite) set of discrete moments

$$\sum_{pi} N^{eq}_{spi}=n_s, \quad \sum_{pi} N^{eq}_{spi}\mathbf{c}_{pi}=n_s\mathbf{v}_s,$$

$$\sum_{pi} N^{eq}_{spi}c_{pi\alpha}c_{pi\beta}=n_s\theta_s\delta_{\alpha\beta}+n_s\nu_{s,\alpha}\nu_{\beta,s},$$

$$\sum_{pi} N^{eq}_{spi}c_{pi\alpha}c_{pi\beta}c_{pi\gamma}=n_s\theta_s[\nu_{s,\alpha}\delta_{\beta\gamma}\cdots]+n_s\nu_{s,\alpha}\nu_{s,\beta}\nu_{s,\gamma},$$

$$\sum_{pi} N^{eq}_{spi}c_{pi\alpha}c_{pi\beta}\mathbf{c}^2_{pi}=4n_s\theta^2_s\delta_{\alpha\beta}+n_s\theta_s\mathbf{v}^2_s\delta_{\alpha\beta}+6n_s\theta_s\nu_{s,\alpha}\nu_{s,\beta} + n_s\nu_{s,\alpha}\nu_{s,\beta}\mathbf{v}^2_s \tag{23}$$

are those satisfied (in the continuum limit) by the Maxwellian g_s; and similarly for the cross-species $N^{eq}_{ss'pi}$ and the continuum limit cross-species Maxwellian $g_{ss'}$ defined in Eq. (9).

Now the only way the macroscopic species velocity $\mathbf{v}_s$ can arise on the right-hand side of Eq. (23) is if it so appears in the expansion form of N^{eq}_{spi} in Eq. (22). Thus, for example, if we invoked moment closure at the third moment, then the Taylor expansion of N^{eq}_{spi} must include all appropriate combinations of $\mathbf{v}_s$ up to terms of $O(v^3_s)$, as is done in the explicit expansion of Eq. (22). On the other hand, if one pushed for closure at the fourth moment, one would need to include terms of $O(v^4_s)$ in Eq. (22). In this paper, we invoke closure at the third moment and defer further comments on this to the Conclusion section.

On substituting Eq. (22) into (23) one must evaluate the lattice geometry-dependent basis moments of the form

$$T^{(n)}_{\alpha\ldots\zeta}=\sum_p T^{(n)}_{p,\alpha\ldots\zeta}=\sum_p\sum_i c_{pi\alpha}\cdots c_{pi\zeta} \tag{24}$$

for the nth moment. Equation (24) consists of $n\mathbf{c}_{pi}$ products. For closure at the third moment, one must evaluate $T^{(n)}$ up to the sixth basis moment tensor, $n=6$. Thus, having chosen closure at the third moment, discrete lattice effects will not pervade the final macroscopic conservation equations if all the basis tensor moments $T^{(n)}$, for n up to 6, are isotropic. Now

$$T^{(4)}_{p,\alpha\beta\gamma\delta}=\psi_p Y_{\alpha\beta\gamma\delta}+\phi_p(\delta_{\alpha\beta}\delta_{\gamma\delta}+\cdots), \tag{25}$$

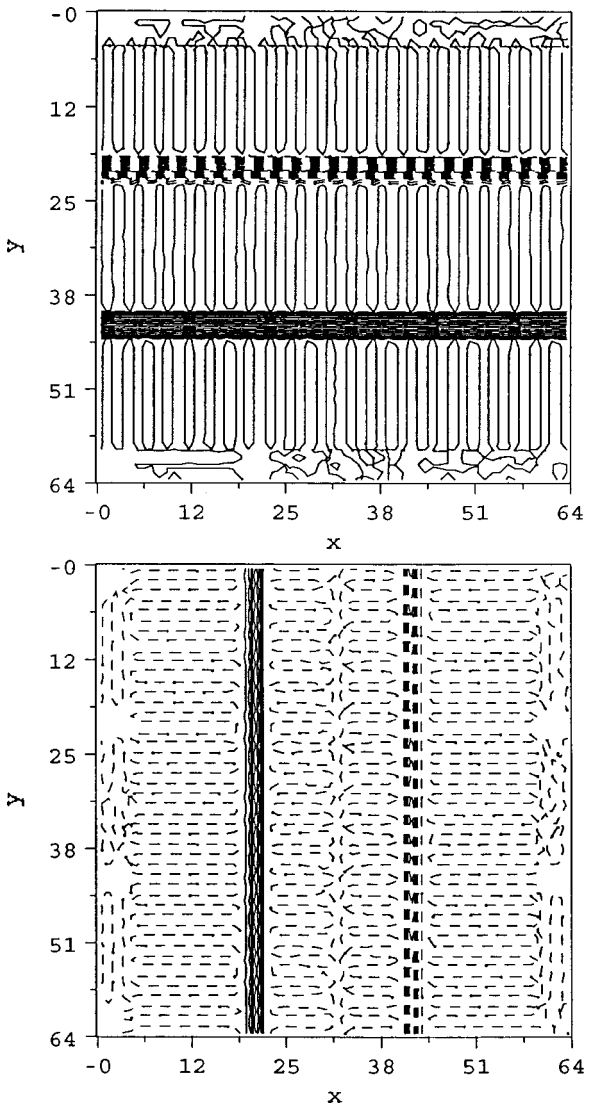

FIG. 1. The initial vorticity layers, ω_1 and ω_2, for the two interacting fluid species. The upper plot is for fluid 1 with $\omega_1 = \omega_1(y)$: solid lines are for positive vorticity while dashed lines are for negative vorticity. The lower plot is the vorticity layers $\omega_2 = \omega_2(x)$ for the more massive and denser fluid 2 ($m_2 = 10m_1$, $n_2 = 3n_1$). Initial species velocity profiles were chosen so that $\max(m_1 n_1 |v_1|) \approx \max(m_2 n_2 |\mathbf{v}_2|)$, which results in $\omega_1 \approx 30\omega_2$, i.e., on a normalized 64×64 mesh (with the simulations themselves being performed on a 256×256 spatial grid), fluid 1 has a negative vorticity layer $\omega_1 = -5.6\times10^{-2}$ for $20<y<23$ and a positive vorticity layer $\omega_1 = 6.3\times10^{-2}$ for $41<y<44$. Similarly, for fluid 2, the vorticity layers are $\omega_2 = 2.4\times10^{-3}$ for $20<x<23$ and $\omega_2 = -2.4\times10^{-3}$ for $41<x<44$.

$$T^{(6)}_{p,\alpha\beta\gamma\delta\varepsilon\zeta} = \Psi_p Y_{\alpha\beta\gamma\delta\varepsilon\zeta} + \Lambda_p(\delta_{\alpha\beta} Y_{\gamma\delta\varepsilon\zeta} + \cdots) + \Phi_p(\delta_{\alpha\beta} T^{(4)}_{\gamma\delta\varepsilon\zeta} + \ldots), \tag{26}$$

where $Y_{\alpha\beta\gamma\delta\cdots}$ is the higher dimension Kronecker tensor and is anisotropic. Only the 2D Kronecker tensor $\delta_{\alpha\beta}$ is isotropic. The parameters $\psi_p, \phi_p, \ldots$ are dependent on the particularly chosen lattice geometry.

For a square lattice, $\psi_p \neq 0$. Thus even $T^{(4)}_{p,\alpha\beta\gamma\delta}$ is anisotropic for any p. Thus to enforce both $T^{(4)}_{\alpha\beta\gamma\delta}$ and $T^{(6)}_{\alpha\beta\gamma\delta\varepsilon\zeta}$ one must choose p sufficiently large as well as an imposition of

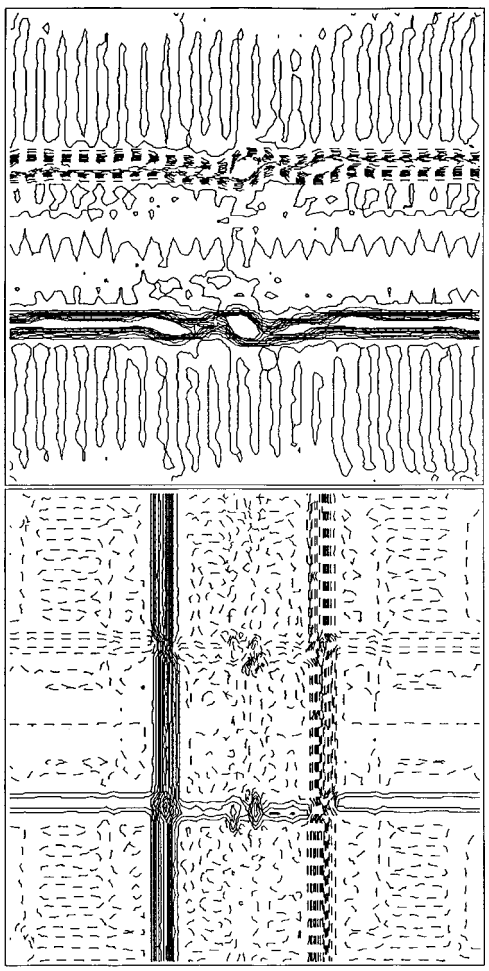

FIG. 2. The vorticity layers after 1000 TLBM time steps ($t = 1$ K). The vorticity layers retain their identities, but fluid 1 (upper plot) already shows the formation internal vortices. The vorticity strengths are fluid 1 (upper plot), $-3.6\times10^{-2}<\omega_1<3.5\times10^{-2}$; fluid 2 (lower plot), $-2.2\times10^{-3}<\omega_2<2.2\times10^{-3}$.

constraints on the distribution function expansion coefficients $A_{sp}, \ldots$ in Eq. (22). For the TLBM parameter range of interest to us, we have found the square lattice to be extremely numerically unstable [9].

Now the hexagonal lattice has a higher symmetry, and this is reflected in the fact that now $\psi_p = 0$. Thus $T^{(4)}_{p,\alpha\beta\gamma\delta}$ is automatically isotropic while $T^{(6)}_{p,\alpha\beta\gamma\delta\varepsilon\zeta}$ is anisotropic at each speed p. Unfortunately [10], for the hexagonal lattice, one cannot form composite lattices that will enforce the isotropy of $\sum_p T^{(6)}_{p,\alpha\beta\gamma\delta\varepsilon\zeta}$. For the square lattice, however, one can achieve isotropy of $\sum_p T^{(6)}_{p,\alpha\beta\gamma\delta\varepsilon\zeta}$ for p sufficiently large [10]—but we have found this representation to be extremely numerically unstable. Thus, the simulations reported here have been performed on the hexagonal lattice, with the coefficients $A_{sp}, \ldots$ being those determined by Alexander, Chen, and Sterling [9]. While this will introduce some higher-order (macroscopic) nonlinearities into the momentum and energy equations [10], these should play a negligible role in our present free-decay simulations since the flow Mach number is quite low. We are currently working on the octagonal lattice representation, in which the isotropy of

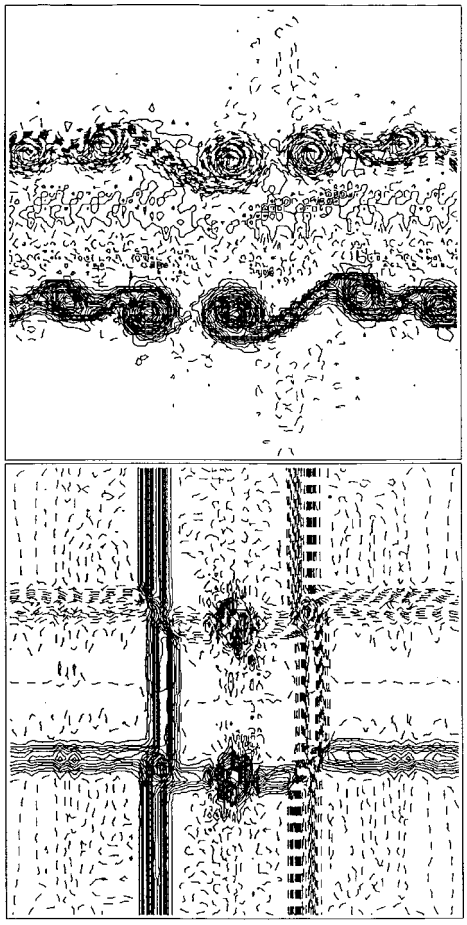

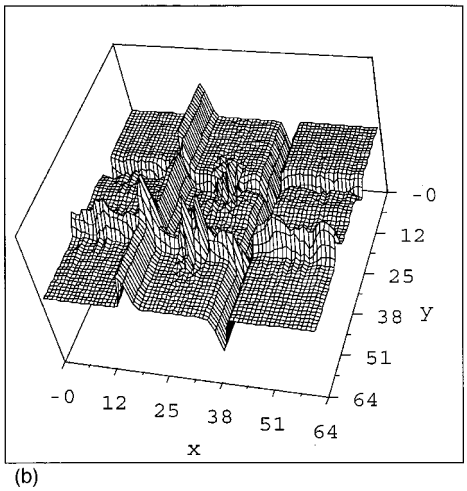

FIG. 3. (a) The vorticity contours at $t=2$ K. The fluid 1 (upper plot) layers have given way to individual vorticies, while the more massive fluid 2 still retains its vorticity layers, but now shows the influence of the coupling to fluid 1. The vorticity strengths are fluid 1 (upper plot), $-2.0\times10^{-2}<\omega_1<2.1\times10^{-2}$; fluid 2 (lower plot), $-2.2\times10^{-3}<\omega_2<2.2\times10^{-3}$. (b) The corresponding $t=2$ K total (density weighted) vorticity $\omega_{\mathrm{tot}}(\mathbf{x})=[n_1(\mathbf{x})m_1\omega_1(\mathbf{x})+n_2(\mathbf{x})m_2\omega_2(\mathbf{x})]/[n_1(\mathbf{x})m_1+n_2(\mathbf{x})m_2]$.

$\Sigma_p T^{(6)}_{p,\alpha\beta\gamma\delta\varepsilon\zeta}$ can be enforced and thereby eliminate the spurious higher-order nonlinearities. Moreover, based on the linear octagonal stability analyses [15] we expect this representation to be quite numerically stable. These results will be reported on in the near future.

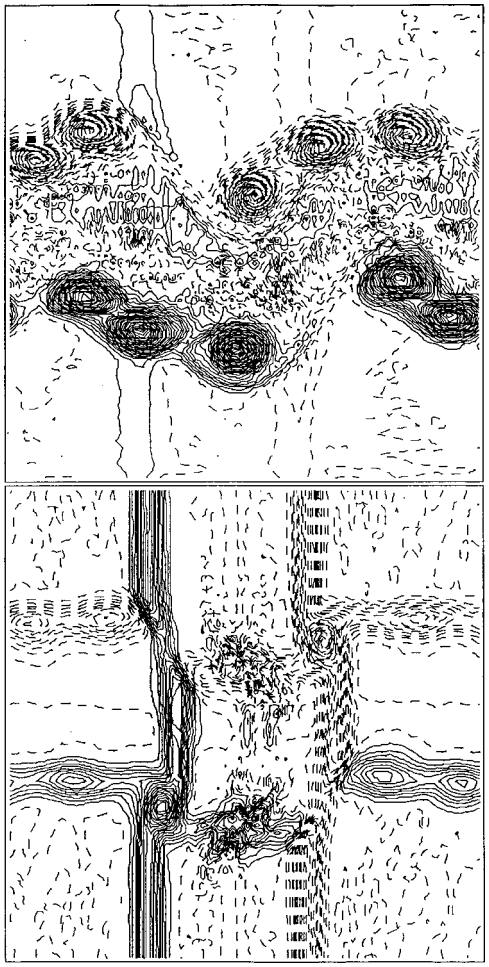

FIG. 4. The vorticity contours at $t=4$ K. The merging of like-signed vorticies is beginning to occur for fluid 1 (upper curve). The vorticity strengths are fluid 1 (upper plot), $-7.1\times10^{-3}<\omega_1<6.8\times10^{-3}$; fluid 2 (lower plot), $-2.1\times10^{-3}<\omega_2<1.9\times10^{-3}$.

It should now be apparent as to what some of the difficulties are facing the TLBM: The discrete distribution functions, Eq. (22), must be non-Maxwellian in order to remove discrete velocity lattice effects. With the loss of an H theorem, one is faced with numerical instabilities.

III. 2D TWO-SPECIES DOUBLE VELOCITY SHEAR TURBULENCE

We consider the free-decay of a two-species system ($m_2=10m_1, n_2=3n_1$) in which there are horizontal velocity shear layers in fluid 1 interacting with weak vertical shear layers in fluid 2. Initially, the mean velocity of fluid 1 is chosen to be an order of magnitude greater than the mean velocity in fluid 2, with fluid 1 having an initial Reynolds number Re=20 000, a factor of over 25 greater than that in fluid 2. Thus the lighter fluid 1 is turbulent while the heavier fluid 2 is laminar. In fact, if the species were uncoupled, the fluid 2 vortex layers would undergo viscous decay and diffusion because of its low Reynolds number. The simulations were performed on a 256×256 spatial grid, with periodic boundary conditions and with $\tau_{11}=0.5056$, $\tau_{12}=9438$, $\tau_{12}=0.507$, and $\tau_{22}=278\,668$. The plots are shown on a rescaled 64×64 mesh.

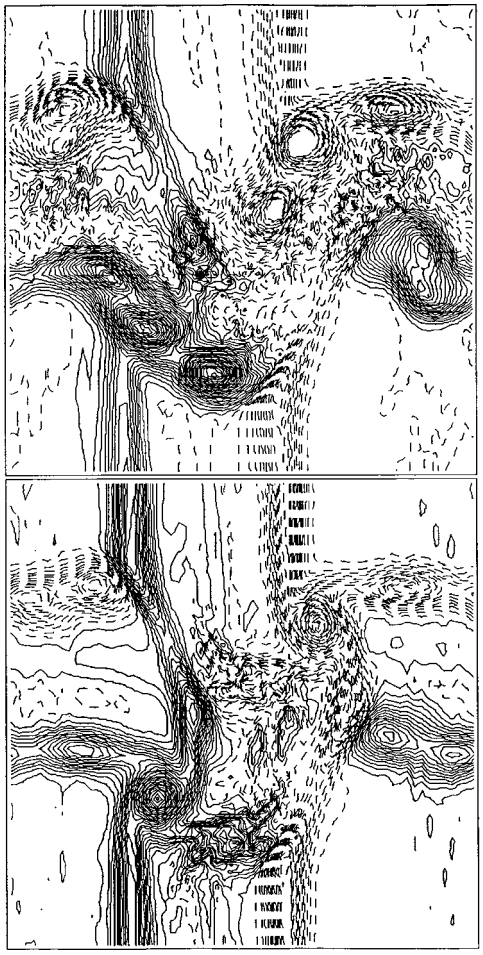

FIG. 5. The vorticity contours at $t=7$ K. There is now strong influence of one species on the other for both fluids 1 and 2. The geometry of the merging vortices in fluid 1 tends to rotate them into the direction of the initial vertical layers of fluid 2. These layers are still quite evident in fluid 2. The vorticity strengths are fluid 1 (upper plot), $-1.9(-3)<\omega_1<1.7(-3)$; fluid 2 (lower plot), $-1.6(-3)<\omega_2<1.6(-3)$.

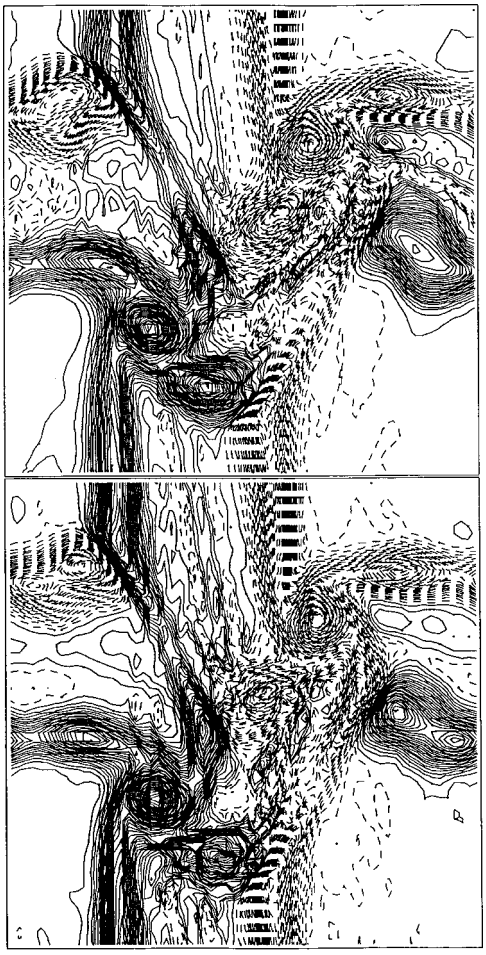

FIG. 6. The vorticity contours at $t=9$ K. Equilibration of nearly all vortex structures in fluid 1 and fluid 2 has now occurred. The vorticity strengths have equilibrated, with fluid 1 (upper plot), $-1.4\times10^{-3}<\omega_1<1.4\times10^{-3}$; fluid 2 (lower plot), $-1.4\times10^{-3}<\omega_2<1.4\times10^{-3}$.

The initial vorticity contour plots for fluid 1 (upper plot) and fluid 2 (lower plot) are shown in Fig. 1 after the application of a 1% perturbation to the velocity fields. Positive and negative vorticities will be represented throughout by solid and dashed curves. It should be noted that the initial vorticity ranges for the two fluids are quite disparate:

$$\text{Fluid } 1: -5.6\times10^{-2}<\omega_1<6.3\times10^{-2},$$

$$\text{Fluid } 2: -2.4\times10^{-3}<\omega_2<2.4\times10^{-3}.$$

By 1 K time steps (with a fluid 1 eddy turnover time being $\approx$400 TLBM time steps, based on the initial velocity magnitude) the vorticity layers in the lighter fluid 1 have become unstable with co- and counter-rotating vortices forming within their respective vortex layers. The vorticity layers of fluid 2 do not yet exhibit any internal structures, while the coupling between fluid 1 and fluid 2 results in an imprinting of the major fluid 1 localized vorticies in fluid 2—see Fig. 2. These internal vortex structures in fluid 1 now become the dominant feature instead of the initial vortex layer itself by $t=2$ K, Fig. 3(a). For fluid 2, dominant due to its initially low Reynolds number, the vertical vortex layer structures are still dominant. However, due to the fluid-fluid coupling, vortex structures have now formed. In particular, the constructive interference between the positive vortex layer of fluid 1 and that of fluid 2 results in an imbedded co-rotating vortex at $(x,y)=(21,42)$ and an imbedded counter-rotating vortex at (42, 21), relative to the axes labeling in Fig. 1. These imbedded vortices are over 50% stronger than the imprinted co- and counter-rotating vortices at (31, 43) and (31, 22), respectively In Fig. 3(b), the total (density weighted) vorticity surface is plotted at $t=2$ K.

By $t=4$ K (Fig. 4), the fluid 1 individual vortices are beginning to merge with spatial locations no longer determined by the initial horizontal layers. The vortex structure for fluid 2 is similar to that at $t=1$ K. In Fig. 5, at $t=7$ K, the vortex structures in fluid 1 and fluid 2 are becoming similar. In particular, fluid 1 now exhibits marked effects of the vertical vortex layers of fluid 2 while its vortex-merging structures rotate more and more towards the vertical. The fluid 2 vortex pattern, however, continues to be dominated by two large vortices situated within the vertical layers—and these two vortices (one co- and the other counter-rotating) have the same spatial location as for $t=4$ K to within 5%.

The vortex structures in fluids 1 and 2 have become quite

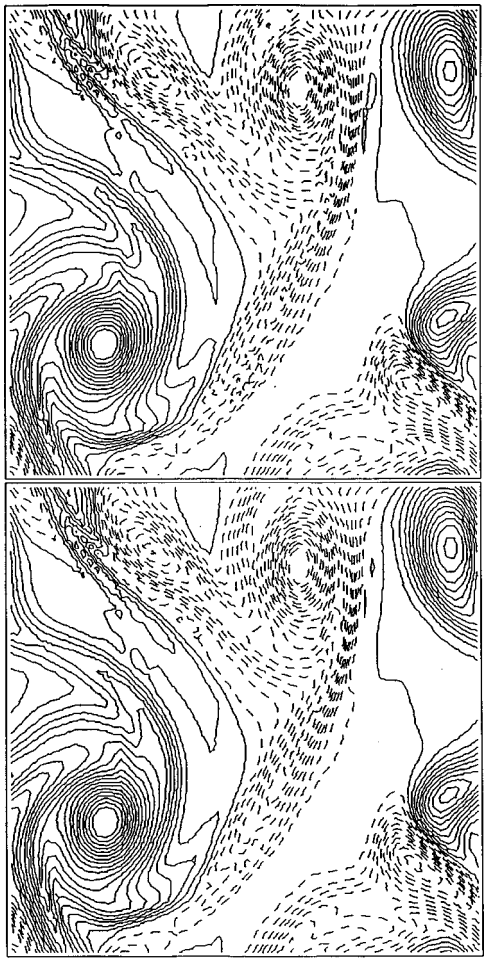

FIG. 7. The vorticity contours at $t=30$ K. The system is evolving slowly towards the final relaxed state. The initial vortex layers have been replaced by individual vortices whose strengths are fluids 1 and 2, $-4.5\times10^{-4}<\omega_{1,2}<4.5\times10^{-4}$.

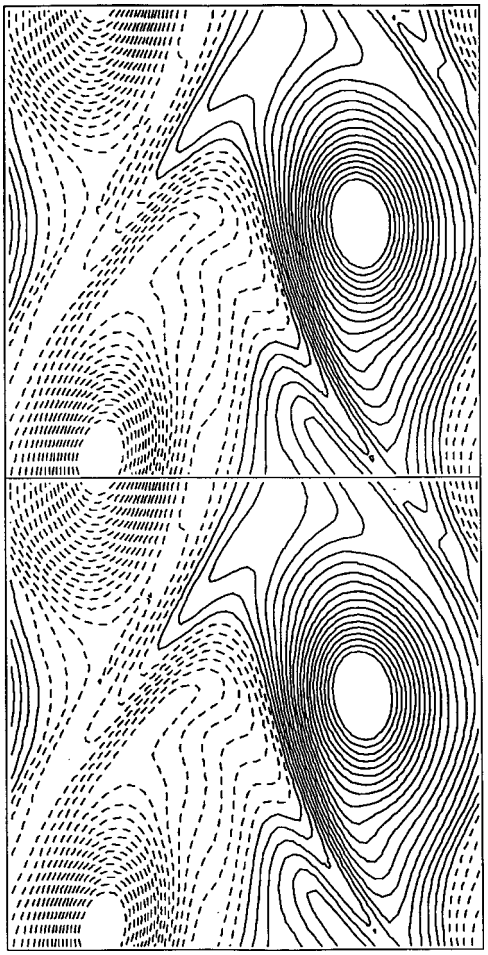

FIG. 8. The vorticity contours at $t=109$ K. The system is close to the final relaxation states of one large vortex (solid curve) with $\omega>0$ and one large vortex (dashed curve) with $\omega<0$. Vortex strengths are fluids 1 and 2, $-4.5\times10^{-4}<\omega_{1,2}<4.5\times10^{-4}$.

mode locked to each other, even in magnitudes, by $t=9$ K, Fig. 6. At $t=30$ K, Fig. 7, the initial vortex layer structures are no longer evident, and global vortex structures are dominant, with the spatial locations of these dominant vortices being not more than 12% from their positions at $t=4$ K. One moves quite close to the final relaxed state of one co-rotating and one counter-rotating vortex by $t=109$ K, Fig. 8.

The temperature surfaces relax even slower than the vortex surfaces, as expected from simple kinetic theory arguments [1]. Initially, one has peaked temperature profiles for each species, parallel to their species initial vortex layers, i.e., $\theta_1=\theta_1(y)$, while $\theta=\theta_2(x)$. There is little change in the peak temperature profiles by $t=1$ K, Fig. 9. The temperature profiles for fluid 1 and fluid 2 are still very different from each other at $t=9$ K (Fig. 10) in contrast to the fluid vorticities that have already equilibrated with each other, Fig. 6. However, by $t=30$ K (Fig. 11) there is global equilibrium and much of the local temperature profile features have equilibrated. Total temperature equilibration for the two species has been achieved by $t=60$ K (Fig. 12)—but it is difficult to quantitatively correlate the vorticity surfaces to the corresponding temperature surfaces. Qualitatively, however, one can usually find peaks in the temperature profiles at the corresponding vorticity minima, and vice versa.

IV. CONCLUSIONS

We have considered the equilibration and relaxation of a 2D turbulent binary system using the TLBM, an extremely efficient and highly parallel and vector algorithm. As discussed by Morse [1], for a spatially homogeneous system, the velocity equilibration time for the two species is given by

$$\frac{\partial}{\partial t}(\mathbf{v}_s-\mathbf{v}_{s'})=-\alpha_{ss'}\left(\frac{1}{n_s m_s}+\frac{1}{n_{s'}m_{s'}}\right)\frac{m_s+m_{s'}}{2}(\mathbf{v}_s-\mathbf{v}_{s'}), \tag{27}$$

while the temperature equilibration time for the two species is given by

$$\frac{\partial}{\partial t}(\theta_s-\theta_{s'})=-\alpha_{ss'}\left[(\theta_s-\theta_{s'})\left(\frac{1}{n_s}+\frac{1}{n_{s'}}\right)+\frac{(\mathbf{v}_s-\mathbf{v}_{s'})^2}{3}\left(\frac{m_s}{n_{s'}}-\frac{m_{s'}}{n_s}\right)\right] \tag{28}$$

under the approximation $5(\mathbf{v}_s-\mathbf{v}_{s'})^2<(\theta_s/m_s)+(\theta_{s'}/m_{s'})$. $\alpha_{ss'}$ is given by Eq. (16). Thus, to leading order, the velocity equilibration time is

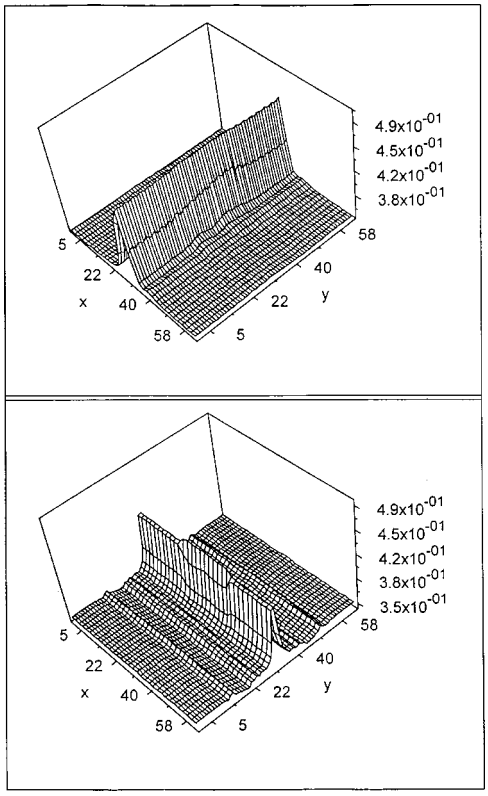

FIG. 9. The temperature profiles $\theta_{1,2}$ at $t=1$ K for fluid 1 (upper plot) and fluid 2 (lower plot). Initially, there are sharp peaks with $\theta=\theta_1(x)$ and $\theta_2=\theta_2(y)$.

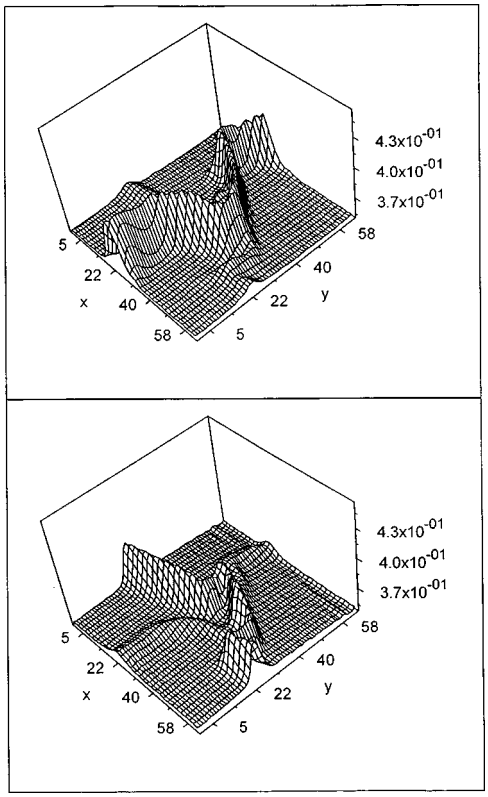

FIG. 10. The temperature profiles at $t=9$ K, a time at which there is almost total equilibration of the vorticity surfaces for fluid 1 and 2: $\omega_1(x,y;t=10\,\mathrm{K})\approx\omega_2(x,y;t=10\,\mathrm{K})$, see Fig. 6. There is some similarity in the temperature profiles; The spatial locations where $\theta_1(x,y)-\theta_0>0$ for fluid 1 are basically the same as those where $\theta_2(x,y)-\theta_0>0$ for fluid 2, Here θ_0 is the base temperature. The temperature magnitudes are, however, significantly different and are biased by the initial profiles.

$$\frac{1}{\tau_{\Delta\nu}}=\alpha_{ss'}\left(\frac{1}{n_s m_s}+\frac{1}{n_{s'}m_{s'}}\right)\frac{m_s+m_{s'}}{2},$$

while the temperature equilibration time is

$$\frac{1}{\tau_{\Delta\theta}}=\alpha_{ss'}\left(\frac{1}{n_s}+\frac{1}{n_{s'}}\right).$$

One thus has the order of magnitude estimate [1]

$$\frac{\tau_{\Delta\theta}}{\tau_{\Delta\nu}}\approx\frac{1}{2}\left(\frac{n_1m_1+n_2m_2}{n_1+n_2}\right)\left(\frac{m_1+m_2}{m_1m_2}\right)$$

for the relative equilibration times for the disappearance of temperature differences between the two species compared to that for the mean velocity differences. This estimate is independent of spatial dimension since Morse was considering pure collisional relaxation in a spatially homogeneous system. For the parameters considered here ($m_2=10m_1$, $n_2=3n_1$, and initially $\nu_1=30\nu_2$) this order-of-magnitude estimate $\tau_{\Delta T}\approx 4\tau_{\Delta\nu}$ agrees well with the TLBM spatially inhomogeneous simulation result of $\tau_{\Delta T}\approx 3.3\tau_{\Delta\nu}$, cf, Figs. 6 and 12. The reason that the role of spatial dimension is suppressed in our simulation is that the heavier fluid 2, if uncoupled from the turbulent fluid 1, is laminar, with the temperature profile undergoing simple linear decay and diffusion. However, on increasing the Reynolds number of fluid 2 (e.g., increasing ν_2) so that its flow becomes turbulent (in the sense that its temperature profile undergoes significant nonlinear modifications), then the equilibration ratio for the coupled system no longer follows the Morse prediction and spatial dimensionality becomes important.

A reason for our continued interest in the TLBM is its possible role in studying the scrape-off-layer in a tokamak. In this region, there are time varying spatial domains in which the neutral particle collisionality ranges from highly collisional (fluid) to the kinetic (Monte Carlo) regime. While attempts are being made to couple plasma-fluid codes to Monte Carlo codes, this coupling is necessarily numerically stiff due to the disparate length and time scales involved in the these schemes. On the other hand, a coupling of the TLBM with Monte Carlo codes should be more straightforward since both schemes are kinetic. It is also possible, as suggested by some (Ref. [21]), that one may be even able to utilize the TLBM algorithm even in the weakly collisional Monte Carlo regime. Then the TLBM algorithm would itself cover the whole collisionality regime-albeit with appropriately modified collision operators.

The major hurdle facing the extensive use the TLBM is its numerical instability when wide parameter regimes are considered. Considerable research is underway to obviate this, but the root of the problem is clear: If one introduces discrete phase space velocity lattices, one is forced to consider relaxation distribution functions that must be non-Maxwellian. The number of constraints needed to be enforced on N^{eq} is reduced as one moves to higher isotropy lattice. In particular,

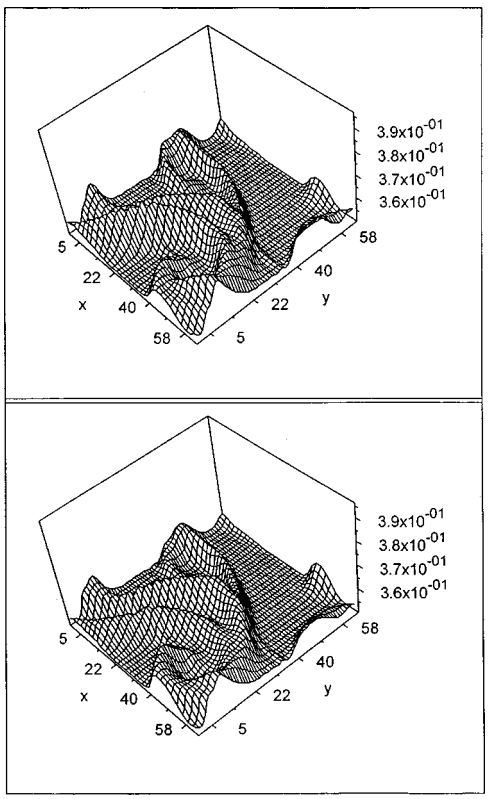

FIG. 11. The temperature profiles at $t=30$ K. Temperature equilibration between the two species is almost complete.

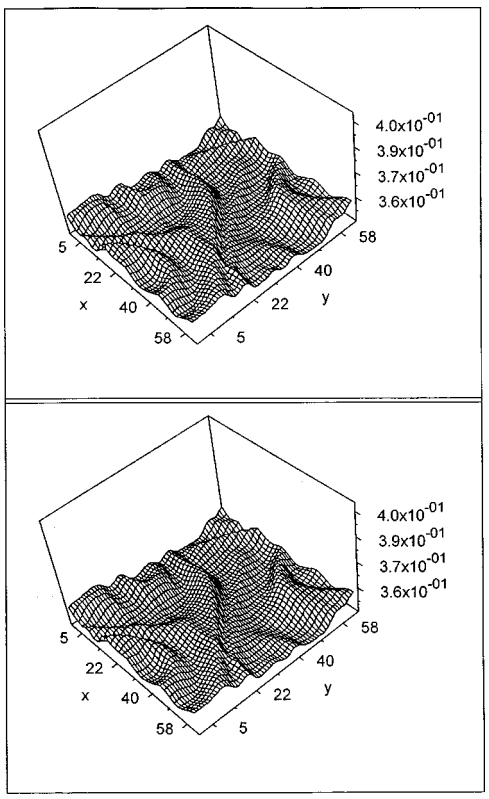

FIG. 12. The temperature profiles at $t=60$ K. Temperature equilibration between the two species is now complete.

the hexagonal lattice is more stable than the square lattice [13] while the octagonal lattice (with its inherent $T^{(6)}_{p,\alpha\beta\gamma\delta\epsilon\zeta}$ isotropy) is more stable than the hexagonal [15]. However, since the octagonal lattice is no longer space filling the spatial grid is necessarily uncoupled from the velocity lattice. This uncoupling requires an extra step to be incorporated into the TLBM algorithm—an interpolation procedure that couples the free-streaming with the nodes of the chosen spatial grid [13]. Even if one employed lower symmetry space-filling lattices, it would still be necessary to introduce interpolation if nonuniform spatial grids are employed (e.g., for wall-bounded flows). We are currently looking into employing temperature-dependent velocity lattices, and will present these results elsewhere.

ACKNOWLEDGMENTS

The computations presented here were performed on the NERSC J90's and T3E as well as on NASA Goddard's T3E.

[1] T. F. Morse, Phys. Fluids **6**, 1420 (1963).
[2] T. F. Morse, Phys. Fluids **7**, 2012 (1964).
[3] B. B. Hamel, Phys. Fluids **8**, 418 (1965).
[4] L. H. Holway, Jr., Phys. Fluids **9**, 1658 (1966).
[5] J. M. Greene, Phys. Fluids **16**, 2022 (1973).
[6] A. D. Kotelnikov and D. C. Montgomery, J. Comput. Phys. **134**, 364 (1997).
[7] J. A. Wesson, *Tokamaks*, 2nd ed. (Oxford Science, Oxford, 1997).
[8] H. Grad, in *Rarefied Gas Dynamics*, edited by F. Devienne (Pergamon, London, 1960); L. Spitzer, Jr., *Physics of Fully Ionized Gases*, 2nd ed. (Interscience, New York, 1962), p. 136.
[9] F. J. Alexander, S. Chen, and J. D. Sterling, Phys. Rev. E **47**, 2249 (1993).
[10] Y. Chen, H. Ohashi, and M. Akiyama, Phys. Rev. E **50**, 2276 (1994).
[11] G. McNamara and B. Alder, Physica A **194**, 218 (1993).
[12] G. R. McNamara, A. L. Garcia, and B. J. Alder, J. Stat. Phys. **81**, 395 (1995).
[13] P. Pavlo, G. Vahala, L. Vahala, and M. Soe, J. Comput. Phys. **139**, 79 (1998).
[14] M. Soe, G. Vahala, P. Pavlo, L. Vahala, and H. Chen, Phys. Rev. E **57**, 4227 (1998).
[15] P. Pavlo, G. Vahala, and L. Vahala, Phys. Rev. Lett. **80**, 3960 (1998).
[16] G. Vahala, P. Pavlo, L. Vahala, and N. Martys, Int. J. Mod. Phys. C **9**, 1247 (1998).
[17] G. Vahala, J. Carter, L. Vahala, and P. Pavlo, in Parallel Computational Fluid Mechanics, edited by D. Keyes *et al.* (North Holland, Amsterdam, in press).
[18] P. L. Bhatnager, E. P. Gross, and M. Krook, Phys. Rev. **94**, 511 (1954).
[19] P. Pavlo, G. Vahala, and L. Vahala (unpublished).
[20] J. Sterling and S. Chen, J. Comput. Phys. **123**, 196 (1996).
[21] S. Krasheninnikov (private communication).